Geophysical Journal International

Geophys. J. Int. (2026) **245,** 1–14
Research Paper
https://doi.org/10.1093/gji/ggag096

Estimation of elastic wave properties of tight sandstones using a reformulated digital rock physics method and ultrasonic experiments

Jing Ba,[1] Maozheng Tong,[1] Mengqiang Pang,[2] Ayman N. Qadrouh,[3] Mamdoh Alajmi,[3] José M. Carcione[1,4] and Martin Balcewicz[5]

[1]*School of Earth Sciences and Engineering, Hohai University, Nanjing* 211100*, China.*
[2]*National Key Laboratory of Intelligent Construction and Health Operation of Deep Underground Engineering, China University of Mining and Technology, China. Email: pmengqiang@163.com*
[3]*Carbon Management Institute, King Abdulaziz City for Science and Technology (KACST), PO Box 6086, Riyadh* 11442*, Saudi Arabia*
[4]*National Institute of Oceanography and Applied Geophysics—OGS, Trieste I-*34010*, Italy*
[5]*Bochum University of Applied Sciences (Hochschule Bochum), Am Hochschulcampus 1, D-*44801 *Bochum, Germany.*

Accepted 2026 February 28. Received 2026 February 27; in original form 2025 December 15

SUMMARY

Tight sandstone reservoirs, as a sort of widely distributed unconventional hydrocarbon resource, are characterized by complex microstructural features that give rise to intricate elastic wave responses. In this study, we estimate the wave properties of tight sandstones using a reformulated digital rock physics method. Nine tight sandstone cores from the Sichuan and Ordos Basins in China are selected for X-ray diffraction and ultrasonic measurements under varying pressures and fluid saturations. Variations in elastic wave velocities with respect to effective pressure are analysed for both gas and water saturation. Computed tomography (CT) scans at two resolutions are conducted to reconstruct multiphase digital rocks and investigate the effects of mineral boundaries (MB). Numerical simulations using the finite element and finite difference methods are then performed and compared with the ultrasonic data. The results show that the simulations can effectively estimate elastic properties when accounting for the effects of MB. Furthermore, the resolution of CT scans determines the scale of microstructures captured, which in turn dictates the pressure range over which the numerical simulations produce valid results. The findings indicate that the wave responses derived from these simulations are intrinsically linked to the scan resolution.

Key words: Elasticity and anelasticity; Finite element method; Image processing; Numerical modelling; Acoustic properties; Wave propagation.

1 INTRODUCTION

Tight sandstone reservoirs are a key component of global unconventional hydrocarbon resources, characterized by low porosity and permeability. Their complex microstructural features influence elastic wave propagation, creating challenges in interpreting seismic responses and quantifying reservoir properties. In recent years, digital rock physics (DRP) has demonstrated advantages in quantifying pore structure, modelling multiphase fluid motion and predicting wave responses. The development of tight sandstone reservoirs in China can address the shortage of conventional hydrocarbons and enhance energy security (J. Wang *et al*. 2016; M. Pang *et al*. 2022, 2023; S. Zhang *et al*. 2024). These reservoirs typically exhibit porosity below 10 per cent. However, reservoir heterogeneity causes porosity variations at different depths and zones, so local porosities exceeding 10 per cent in specific rocks do not conflict with the overall tight nature of the reservoir system. *In situ* permeability generally does not exceed 0.1 mD. Their pores primarily consist of secondary dissolved and intergranular pores (C. Zou *et al*. 2012), with poor connectivity and complex distribution patterns, which contribute to the complex mechanisms of elastic wave propagation (Z.Q. Guo *et al*. 2023). Thus, the effective characterization of elastic wave responses is crucial for the development of tight sandstone hydrocarbon reservoirs.

DRP technology can be used to create 3-D models of rocks using Computed tomography (CT) scans, mineral composition analysis and volumetric property analysis (H. Andrä *et al*. 2013a; C. Madonna *et al*. 2013; R. Kadyrov *et al*. 2022). It enables the acquisition of key petrophysical properties such as permeability and elastic moduli (S. Karimpouli & P. Tahmasebi 2016; N. Saxena *et al*. 2019; M. Pang *et al*. 2024, 2025) and has emerged as a complementary approach for rock characterization (H. Andrä *et al*. 2013b; C.F. Berg *et al*.

Table 1. Physical properties of the rock samples.

Samples	A	B	C	D	E	F	G	H	I
Depth (m)	2427.36	2171.08	1980.52	2636.55	1996.8	2228.1	1996	1800	1804
Porosity (per cent)	11.97	3.90	10.10	6.80	4.63	6.45	9.28	8.85	8.24
Dry-rock density ($g\,cm^{-3}$)	2.34	2.32	2.39	2.47	2.44	2.47	2.37	2.41	2.43
Permeability (mD)	0.7294	0.0268	0.2203	0.1705	0.051	0.099	0.205	0.177	0.158

2017; J. Kang *et al*. 2022). The results are particularly effective in analysing pore structures, porosity and permeability. It significantly reduces computational costs and turnaround time compared to traditional experimental approaches.

Numerical simulation methods overcome the limitations of laboratory experimental tests by reproducing the intrinsic relationships among microstructural pore characteristics, interfacial properties and macroscopic elastic responses (Y. Wang & S.S. Rahman 2023). These simulations provide valuable insights into the patterns of oil and gas accumulation (G. Cao *et al*. 2024; J. Li *et al*. 2024), the fluid flow characteristics (H. Wu *et al*. 2021) and the mechanisms of elastic wave propagation (J. Gao *et al*. 2021). A.B. Andhumoudine *et al*. (2021) simulated the effective elastic moduli of coal rocks using a 3-D digital model and finite element method (FEM) and calculated the *P*- and *S*-wave velocities. L. Zhang *et al*. (2019) computed the rock permeability and overcame the limitations of traditional rock physics experiments by simulating fluid flow in the pores of digital cores based on the Navier–Stokes equations. M. Tan *et al*. (2021) investigated the effect of fracture density, fracture opening and fracture length on the carbonate elastic properties of penetrating fractures using CT scans and FEM. E.H. Saenger & S.A. Shapiro (2002) and E.H. Saenger & T. Bohlen (2004) extended the rotated staggered-grid finite-difference method (RSG-FDM) from 2-D elastic media to 3-D viscoelastic anisotropic media, maintaining high accuracy while improving computational efficiency.

Previous studies indicated that simulated elastic wave velocities in rocks are often higher than actual wave velocities (A.B. Andhumoudine *et al*. 2021; J. Zhu *et al*. 2025; M. Pang *et al*. 2025). E.H. Saenger *et al*. (2016) suggested that the discrepancy between numerical and experimental results is primarily due to unresolved features in the original images, particularly at grain contacts. These neglected local heterogeneities may lead to an overestimation of wave velocities in the simulation. Thus, we consider the effects of segmentation and mineral boundaries (MB) on the wave response. Segmentation is the process of identifying different components, or phases, within a 3-D rock image, such as pores, mineral grains and fluids, with a range of grey levels.

To address the issue, we collect two groups of tight sandstone samples from the Sichuan and Ordos Basins in China. X-ray diffraction, cast thin sections (CTS), CT scans at two resolutions, and ultrasonic experiments are used to determine rock properties, as well as wave velocity variations under different effective pressures under gas- and water-saturated conditions. By considering the influences of the representative volume element (RVE), MB and CT scans, a new multiphase digital core was constructed based on the mineral analyses of the samples. Effective elastic simulations are performed using the FEM and FDM, and the results are compared with ultrasonic experimental data at different pressures.

2 EXPERIMENTS

2.1 Rock samples

This study considers four samples (A–D = group I) from the Shaximiao Formation in the Sichuan Basin and five samples (E–I = group II) from the Chang 7 Member of the Yanchang Formation in the Ordos Basin. Both areas are rich in hydrocarbon resources (Q. Chen *et al*. 2007; T. Yang *et al*. 2024). All samples are prepared as standard cylindrical specimens. The diameters of the two groups range from 25.27 to 25.28 mm and 25.08 to 25.15 mm, respectively, with lengths of 49.06 to 49.68 mm and 48.80 to 50.09 mm.

In this study, rock porosity (ϕ) and dry-rock density (ρ_{dry}) are measured using a helium porosimeter and permeability is determined by the unsteady-state pulse transient decay technique (L. Zhang *et al*. 2022). The physical properties of the samples are given in Table 1.

2.2 X-ray diffraction (XRD) and CTS

To further analyse the structural characteristics and mineral compositions of the rocks, CTS and XRD are conducted. The scans enable microscale observation of rock fabric, grain composition and pore types (S. Dong *et al*. 2019). Figs 1 and 2 show the CTS of the two groups under orthogonal and single-polarized light, respectively, indicating a densely packed rock with minute pore spaces and an overall tight structure. The primary pore types are intergranular pores, dissolution pores and microfractures.

We perform XRD measurements to analyse the mineral fractions of the samples (Fig. 3). The sandstone samples from group I (A–D) are mainly composed of quartz, feldspar, cuttings and a small amount of clay, with the cuttings consisting of igneous, metamorphic and sedimentary components. The sandstone samples from group II (E–I) are primarily composed of quartz and feldspar, with small amounts of clay and carbonate minerals (mainly calcite and dolomite).

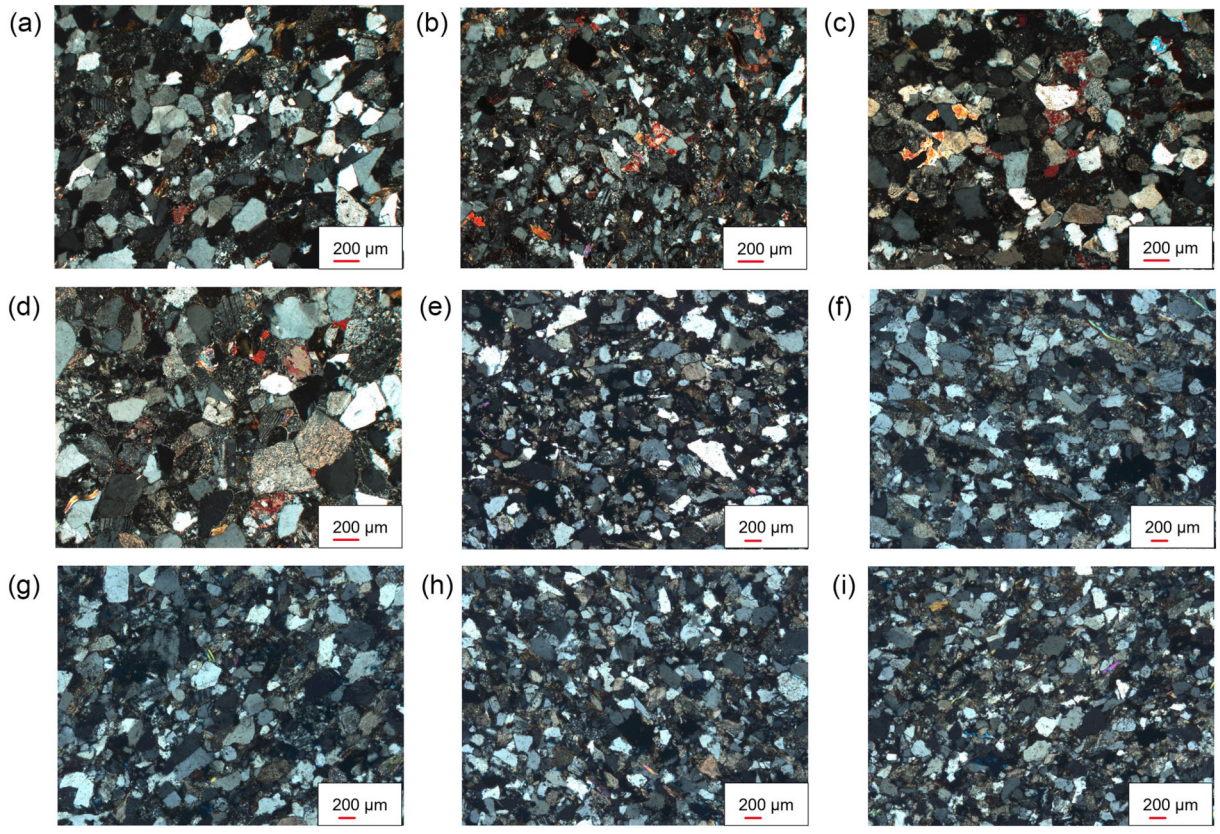

Figure 1. Orthogonal images (cast thin sections) of the rock samples.

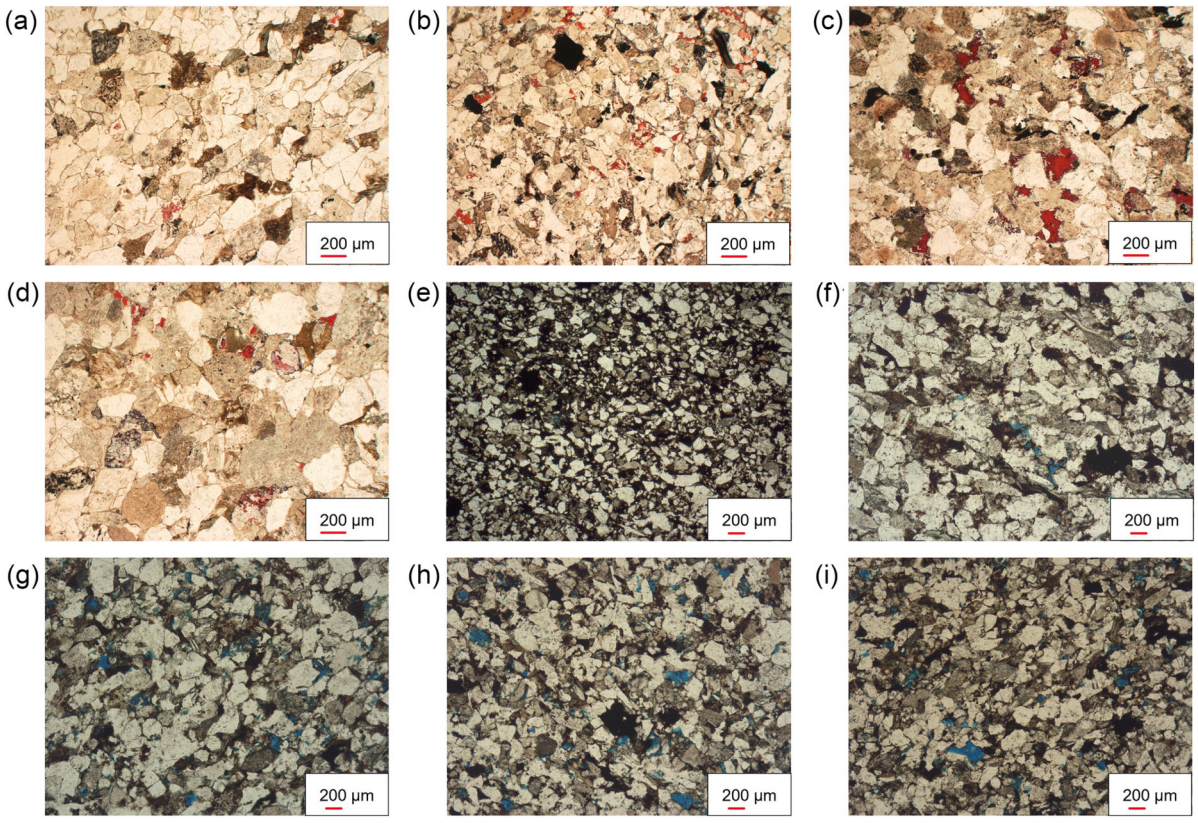

Figure 2. Single polarization images (cast thin sections) of the rock samples.

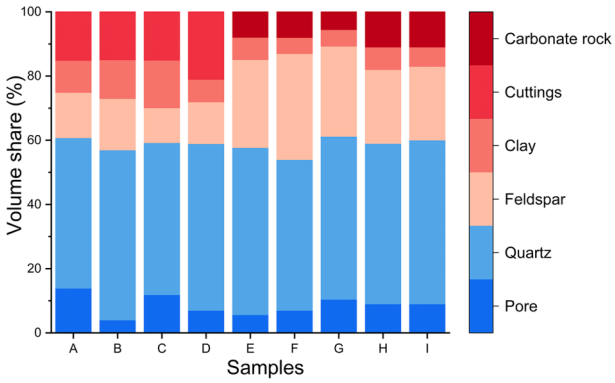

Figure 3. Mineral fractions of two rock sample groups.

2.3 CT scan experiments

CT scans at two resolutions are performed to characterize the core samples and analyse the effects of resolution on numerical simulations. The resolutions for groups I and II are approximately 4 and 16 μm , respectively. The greyscale values of all samples range from 0 to 65 535, corresponding to varying density distributions from air to the rock matrix. The wider greyscale range provides more accurate imaging data for quantitative analysis of physical properties, such as porosity and fractures. 3-D greyscale images of the nine samples are shown in Fig. S1 (Supplementary Material).

2.4 Ultrasonic experiments

We use the ultrasonic pulse transmission method to measure the velocities of elastic waves. The experimental procedure is as follows: Samples are carefully cleaned, dried in a 70 °C oven for 48 hr, then gradually cooled to 25 °C and left to rest for several days before testing. Pressure-dependent elastic property tests are conducted on the two sample groups at confining pressures of 20, 25, 30, 35, 40, 50 and 60 MPa, and 20, 30, 40, 50 and 60 MPa, respectively, with corresponding pore pressures of 10 and 15 MPa. We then measure *P*- and *S*-wave velocities.

Next, the dry samples are placed in a vacuum chamber filled with water and evacuated for 2 hr until no bubbles escape from the specimen surfaces. We confirm full water saturation by comparing the weight of water (the product of the pore volume and fluid density ρ) with that of the sample. Finally, *P*- and *S*-wave velocities are measured at each pressure point using the same procedure as for gas saturation.

2.5 Results

The results are given in Fig. 4, which show that the *P*- and *S*-wave velocities (V_P and V_S) of all samples increase with effective pressure (confining minus pore pressure) at gas- and water-saturated conditions. The increase is mainly due to the closure of pores and microfractures.

It is worth noting that sample B, which has the lowest porosity, also exhibits the lowest V_P and V_S. This may be due to microfractures that are not clearly identified in the CT scans (with a voxel resolution of 4 μm), possibly missing microstructural heterogeneity.

Furthermore, water significantly influences wave velocities. Under the same effective pressure conditions, water-saturated samples have a higher V_P, while V_S remains almost the same. This is consistent with Gassmann's equations (F. Gassmann 1951; J.M. Carcione 2022).

Moreover, the elastic wave velocities of group II (E–I) are slightly higher than those of group I (A–D), which is attributed to differences in mineral composition. Group II has a higher quartz and feldspar content and also contains carbonate minerals (see Fig. 3).

3 CONSTRUCTION OF MULTICOMPONENT DIGITAL CORES

Fig. 5 shows the workflow for constructing a multicomponent 3-D digital core, using the same workflow for both resolutions. Starting with the original CT data, median filtering and threshold segmentation are applied, followed by mineral-boundary (MB) identification, selection of representative volume elements and mineral fraction analysis. This process yields the multicomponent digital core used in subsequent simulations of the elastic properties of tight sandstone.

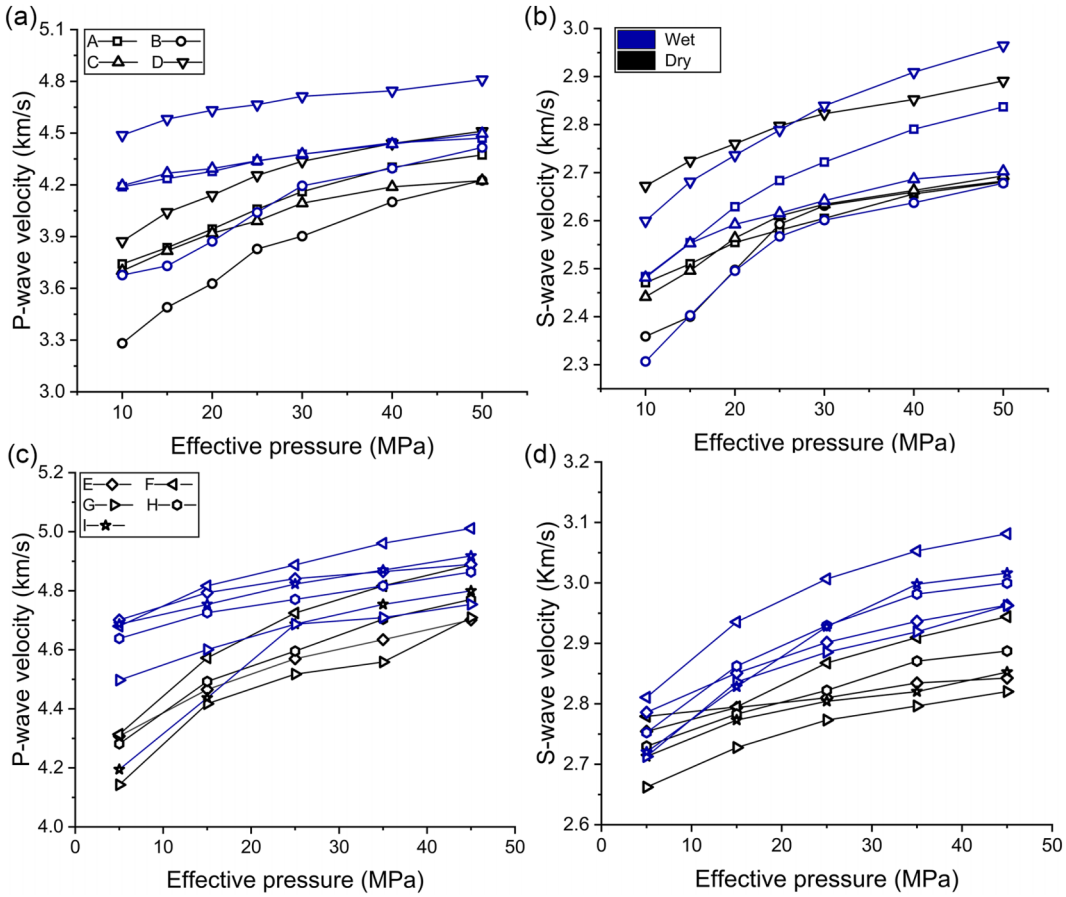

Figure 4. Correlations between effective pressure and *P*- **(a)** and *S*-wave **(b)** velocities for Group I and *P*- **(c)** and *S*-wave **(d)** velocities for Group II, under gas-and water saturation.

3.1 Data pre-processing and threshold segmentation

To process the CT images, we first apply a 2-D iterative median filter (three iterations on XY planes) for noise reduction, followed by normalizing the greyscale histogram to the full 16-bit dynamic range (0–65 535). For multiphase segmentation, initial thresholds are calculated by using the multithreshold Otsu algorithm (N. Otsu 1975). These specific greyscale thresholds are then iteratively fine-tuned until the volumetric fractions of the segmented digital phases match the quantitative mineralogy obtained from the XRD analysis. Group I is classified into pore, clay, cuttings, quartz and feldspar phases, while group II is classified into pore, clay, quartz, feldspar and carbonate minerals.

3.2 Identification of the mineral phases

Previous studies typically assign elastic properties directly to each phase in segmented images, which can result in significant discrepancies between numerical estimates and ultrasonic data. This bias largely arises from microstructural features within the rock that are not taken into account (E.H. Saenger *et al*. 2016). These regions are susceptible to wave propagation.

Moreover, representing them as an independent phase in the numerical simulations helps to more realistically capture the influence of the actual microstructure on the effective elastic parameters and *P*- and *S*-wave velocities, thereby reducing systematic discrepancies between numerical predictions and experimental results. Therefore, we extract the interfaces between the phases.

Specifically, based on the CT images segmented with the thresholds, slight morphological opening and closing operations (by using a 3-D cubic structuring element with a size of three voxels, i.e. $3 \times 3 \times 3$) are applied to optimize the continuity and integrity of the phase boundaries, thereby improving the segmentation accuracy.

For MB, we first construct a binary mask and define candidate boundary voxels as those in the 26-neighbourhood that are adjacent to at least one MB voxel. The gradient vector and magnitude are computed using a 3-D extension of the Sobel operator (I. Sobel 1995; D.A. Hafiz *et al*. 2011; S. Supiyandi *et al*. 2024) to detect edges in the volumetric image data. The gradient vector $\nabla \mathbf{f}$ at each voxel is defined as

$$\nabla \mathbf{f} = \left[G_x \; G_y \; G_z \right]^{\mathrm{T}}, \tag{1}$$

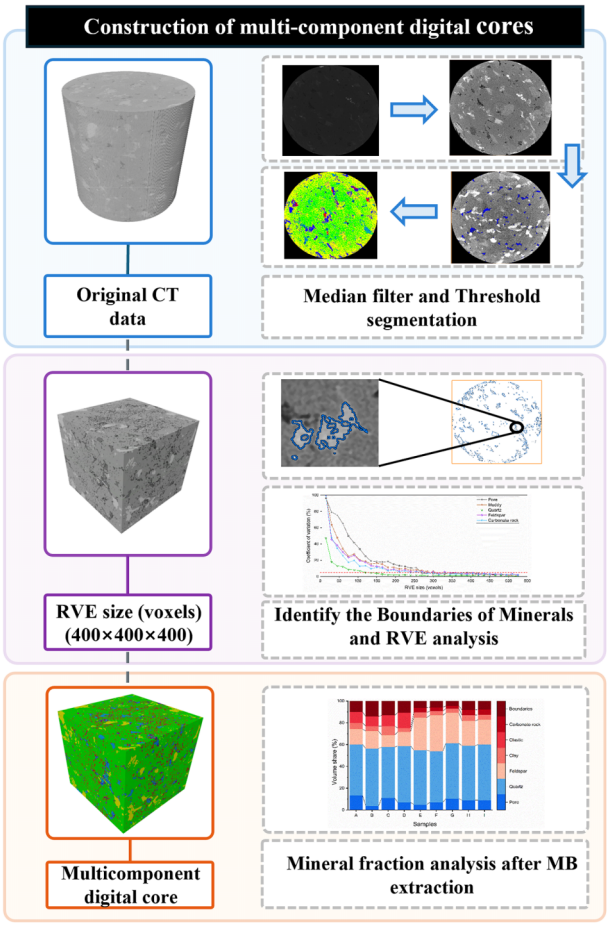

Figure 5. Flowchart of the construction process for the 3-D multicomponent digital core by considering MB.

where G_x, G_y and G_z represent the approximate partial derivatives of the image intensity function f in the x, y and z directions, respectively, obtained via convolution with $3 \times 3 \times 3$ Sobel kernels. The gradient magnitude G at voxel position (n_x, n_y, n_z) is then calculated as:

$$G(n_x, n_y, n_z) = \sqrt{G_x^2 + G_y^2 + G_z^2}. \tag{2}$$

This magnitude quantifies the edge strength, with higher values indicating sharper intensity transitions, which are crucial for subsequent boundary segmentation.

Afterwards, we apply the watershed algorithm (S. Beucher & F. Meyer 2018; R.A. Ketcham 2025) to refine the boundaries, ensuring precise delineation of mineral phases. The watershed algorithm interprets a grey-scale image as a topographic relief, where pixel values represent altitudes. We further adjust the boundaries of these phases by incorporating CTS and XRD measurements. Finally, morphological operations (opening and closing) are used to optimize boundary continuity.

Fig. 6 shows the volume fractions of the components after considering the boundary conditions. The effective moduli of elasticity of these boundary voxels (MB) are set to 10 per cent of the value of the moduli of elasticity of the matrix (skeleton) minerals adjacent to the MB (E.H. Saenger *et al.* 2016; M. Balcewicz *et al.* 2021). This approach accounts for these undetected grain contact below the resolution threshold. Specifically, for the samples in Group I, the MB consists of media between the clay and cuttings and the adjacent matrix minerals, whereas for the samples in Group II, it consists of media between the clay and carbonate minerals and the adjacent matrix minerals.

Subsequently, the effective moduli are calculated using the Voigt–Reuss–Hill averaging method (A. Reuss 1929; R. Hill 1952; W. Voigt 1966; J.M. Carcione 2022). The input properties of all phases are summarized in Table 2 (G. Mavko *et al.* 2020). This approach incorporates boundary specificity while avoiding arbitrary parameter choices.

3.3 Representative volume element analysis

To determine the appropriate RVE, this study extracts multiple cubic subvolumes from the 3-D digital core at random positions for various edge lengths. The coefficient of variation (CV) for each mineral component's volume fraction is calculated to quantify statistical

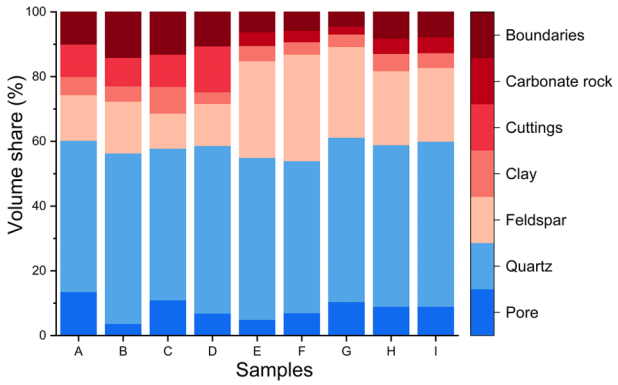

Figure 6. Segmented mineral components of the samples.

Table 2. Elastic properties of each phase.

Phase	Bulk modulus K (GPa)	Shear modulus G (GPa)	Density p (g cm^{-3})
Pores	0.001	0.001	0.32
Clay	6	4	1.57
Cuttings	15	8	2.35
Quartz	37	44	2.65
Feldspar	37	15	2.65
Carbonates	76	32	2.71
Boundary voxels (A–D)	1	0.5	1.96
Boundary voxels (E–I)	3	2	2.14

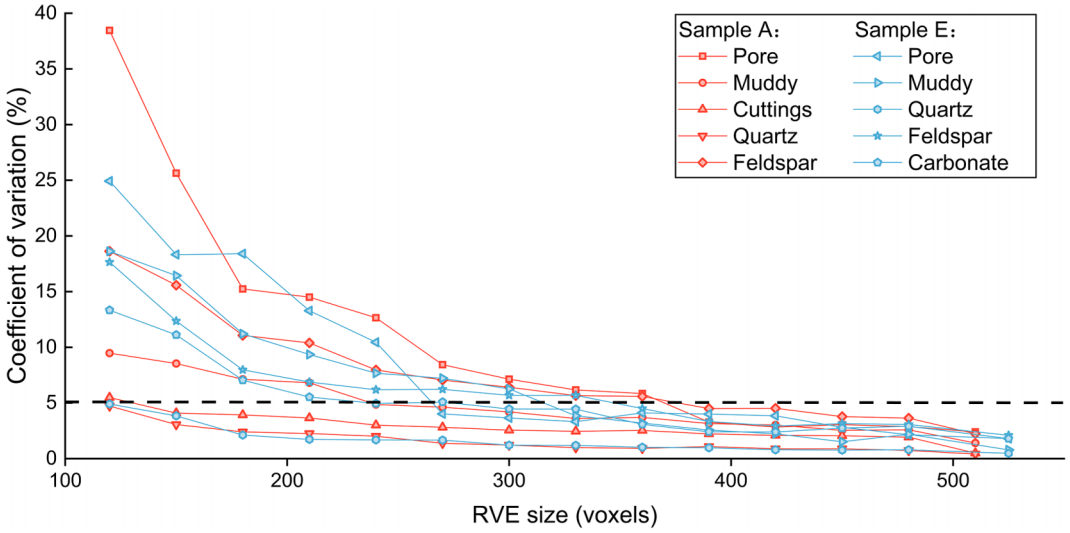

Figure 7. RVE analyses of two samples.

heterogeneity. The volume element is regarded as statistically representative when the CV is below 5 per cent. This threshold is chosen based on the criterion that fluctuations in mineral properties become negligible relative to the mean, indicating that the sample has achieved a macroscopically homogeneous state (N. Saxena *et al.* 2019; M. Balcewicz *et al.* 2021; R. Kadyrov *et al.* 2022).

Fig. 7 shows the relationship between the coefficients of each mineral component and the element size for the samples. It can be observed that the coefficient stabilizes when the cube side length exceeds 300. In this study, RVE with a voxel size of 400 × 400 × 400 is selected. The RVE analysis results for the remaining samples (B–D and F–I) show similar stabilization trends and are provided in Figs S2 and S3 (Supplementary Material).

Fig. 8 presents the 3-D digital core models of the samples.

4 NUMERICAL SIMULATIONS

The FEM and the RSG-FDM are applied to estimate the *P*- and *S*-wave velocities of 3-D digital core models representing tight sandstones.

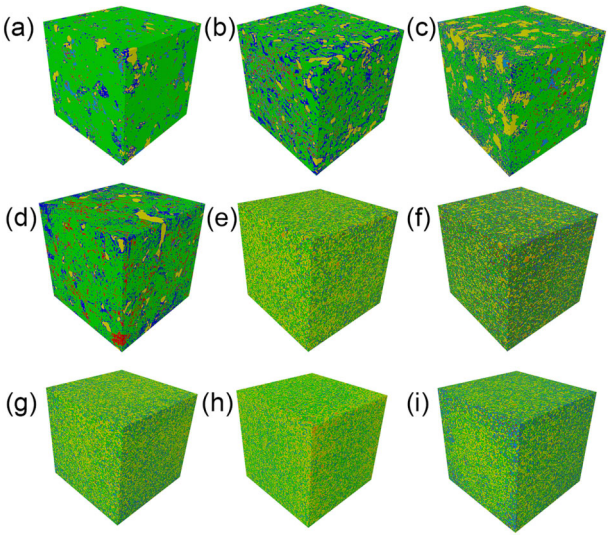

Figure 8. The final constructed 3-D digital cores of the nine samples. Samples A–D have a side length of 1600 μm, while samples E–I have a side length of 6400 μm.

4.1 Finite element method (FEM)

To estimate the elastic wave velocities of the digital cores, we perform a static homogenization analysis using FEM (J.M. Carcione 2022). The simulation domain consists of a grid of 400 × 400 × 400 voxels derived from the segmented digital core. The local elastic properties are assigned to each voxel based on the constituent phases summarized in Table 2.

To balance computational efficiency with prediction accuracy, a single-step mixed loading strategy is used. Simultaneous normal strains ($\varepsilon_{ii} = 1.0 \times 10^{-3}$) and tensor shear strains ($\varepsilon_{ij} = 5.0 \times 10^{-4}$, equivalent to engineering shear strains $\gamma_{ij} = 1.0 \times 10^{-3}$) are applied to the digital volume. This voxel-based FEM workflow remains a standard and robust approach in modern digital rock physics (Y. Alkhimenkov 2025).

Assuming the digital core is macroscopically isotropic, the effective bulk modulus (K) and shear modulus (G) are derived from the volume-averaged stress and strain fields. Consistent with the fundamental averaging principles (R. Hill 1963; R. Ahmad *et al.* 2023), the effective moduli are calculated as

$$K = \frac{\bar{\sigma}_{xx} + \bar{\sigma}_{yy} + \bar{\sigma}_{zz}}{3(\bar{\varepsilon}_{xx} + \bar{\varepsilon}_{yy} + \bar{\varepsilon}_{zz})}, \tag{3}$$

where $\bar{\sigma}_{ii}$ represents the volume-averaged normal stresses.

$$G = \frac{\bar{\tau}_{xy} + \bar{\tau}_{yz} + \bar{\tau}_{xz}}{\bar{\gamma}_{xy} + \bar{\gamma}_{yz} + \bar{\gamma}_{xz}}, \tag{4}$$

where $\bar{\tau}_{ij}$ denotes the volume-averaged shear stresses.

Based on the obtained bulk and shear moduli, V_P and V_S of the 3-D digital core are determined using the standard elastic wave equations (G. Mavko *et al.* 2020)

$$V_P = \sqrt{\frac{K + \frac{4}{3}G}{\rho}}, \tag{5}$$

$$V_S = \sqrt{\frac{G}{\rho}}, \tag{6}$$

where the density ρ is obtained as the weighted average of the component densities.

The global system of linear elastic equations is solved using the preconditioned conjugate gradient method to ensure memory efficiency. The convergence process of the solver is detailed in Fig. S4 (Supplementary Material). The gradient norm and the relative energy change decrease monotonically, indicating that the solution satisfies the first-order optimality conditions and reaches a stable global equilibrium state.

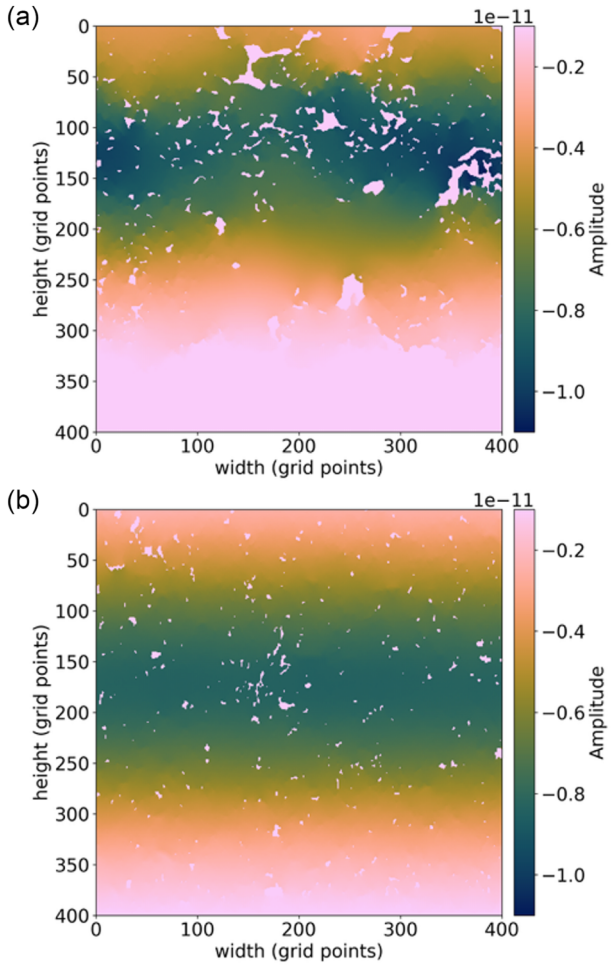

Figure 9. 2-D snapshots of the vertical displacement wavefield at time $t = 0.204$ μm during the numerical simulation for **(a)** Sample A and **(b)** Sample E.

4.2 Finite difference method (FDM)

The rotated staggered-grid finite-difference method (RSG-FDM) is used to estimate *P*- and *S*-wave velocities in 3-D digital cores. Where the effective elastic properties are derived by solving the elastodynamic wave equations

$$\rho \frac{\partial^2 u_i}{\partial t^2} = \frac{\partial}{\partial x_j}\left(c_{ijkl}\frac{\partial u_k}{\partial x_l}\right) + f_i \quad (i = 1, 2, 3), \tag{7}$$

where u denotes displacement, c_{ijkl} is the elasticity tensor, f denotes the source, t is time and i indicates the subindices of the spatial variables.

To estimate the effective elastic properties, a digitized rock sample is embedded in a homogeneous elastic medium characterized by stiffness tensor components $c_{11} = 66$ GPa, $c_{44} = 22$ GPa and density $\rho = 2.54$ g cm^{-3}. These parameters are used only to facilitate numerical simulations; they do not represent any internal mineral phases and do not affect the calculated effective wave velocities of the digital core.

The numerical domain consists of $804 \times 400 \times 400$ grid points, with spatial and temporal increments of $dh = 1.48$ μm and $dt = 163$ ps, respectively. A plane source generates either a *P*- or *S*-wave at the top of the model.

The source wavelet is the first derivative of a Gaussian, providing broadband excitation with a dominant frequency of 3.38 MHz. This frequency satisfies the long-wavelength condition, as the wavelength is much larger than the pore size. The simulation uses second-order finite-difference spatial operators and a second-order time-stepping scheme, with periodic boundary conditions applied perpendicular to the wavefront.

Fig. 9 shows a representative 2-D snapshot of the propagating wavefield (sample E). Receiver planes at the top and bottom of the model record these wavefields to measure the time delay of the average plane wave. Comparing this delay with that from a homogeneous reference model yields the effective wave velocities and elastic moduli (E.H. Saenger *et al.* 2000; E.H. Saenger *et al.* 2004).

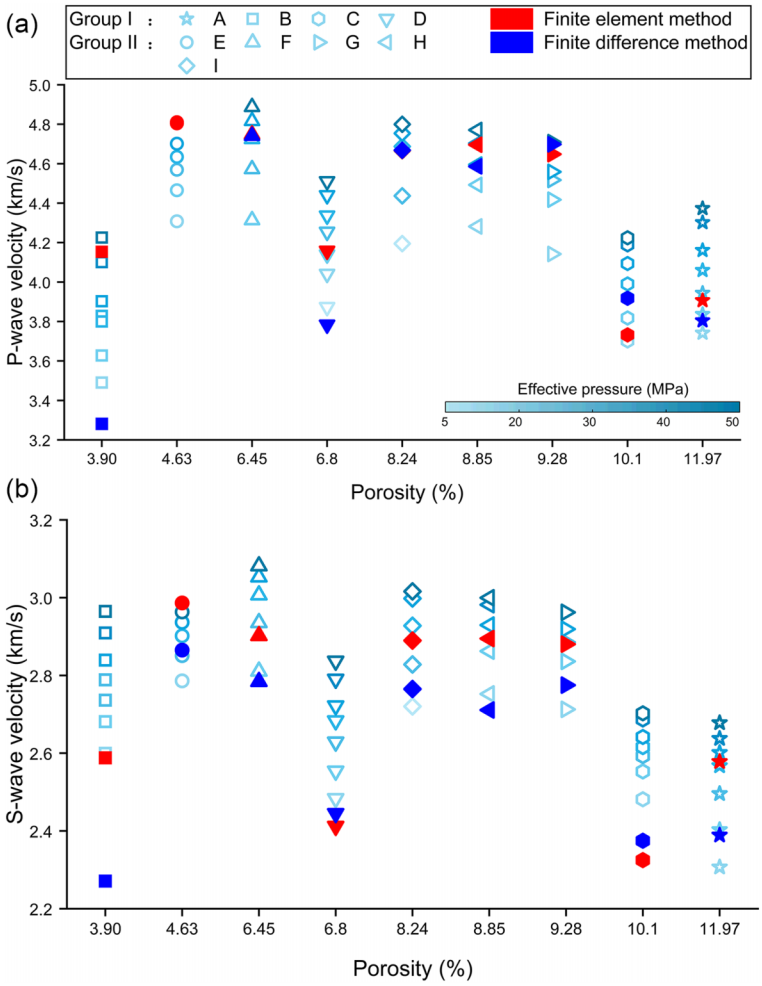

Figure 10. Comparison of simulation results with ultrasonic data at different pressures. *P*- **(a)** and *S*-wave **(b)** velocities.

5 RESULTS

5.1 Simulations

Fig. 10 compares the FEM and FDM results with the experimental data. The simulation falls within the range of the data. The figure also shows the trend of simulated V_P and V_S as a function of porosity. Results indicate that V_P and V_S exhibit a decreasing trend with increasing porosity, though not monotonically. The results indicate that the simulated V_P and V_S generally exhibit a decreasing trend with increasing porosity, but this decrease is not monotonically decreasing.

Notably, Sample B (3.90 per cent porosity) exhibits lower velocities than Sample E (4.63 per cent), deviating from linear trends. This indicates that elastic moduli depend on multiple factors, such as mineral composition and microfractures, rather than solely on porosity. Such complexity highlights the limitations of simple empirical models and validates the necessity of the digital rock physics approach.

Furthermore, we analysed the average values across a range of pressure conditions. The simulations are basically consistent with the mean values of the samples at different pressures (see Fig. S5 in the Supplementary Material). For V_P, the relative errors of the FEM and FDM simulations compared to the experimental averages are 5.44 and 7.50 per cent, respectively, for Group I, and 3.34 and 3.05 per cent for Group II. The corresponding errors for V_S are 4.79 and 10.36 per cent in Group I, and 1.83 and 3.99 per cent in Group II. Based on the reformulated digital core method, accounting for the effects of mineral phases, it can effectively predict elastic wave velocities.

We conduct a correlation analysis between the predicted and experimental values (Fig. 11). The central fitting curve illustrates the linear correlation between the simulations and experiments, where the outer and inner shaded bands represent the prediction and confidence intervals, respectively. The narrower the confidence interval, the more stable the mean estimate. A narrower prediction interval indicates smaller prediction uncertainty and fewer outliers. The coefficient of determination (R^2) of FEM and FDM for the predictions and experiments is 0.968 09 and 0.967 16, respectively.

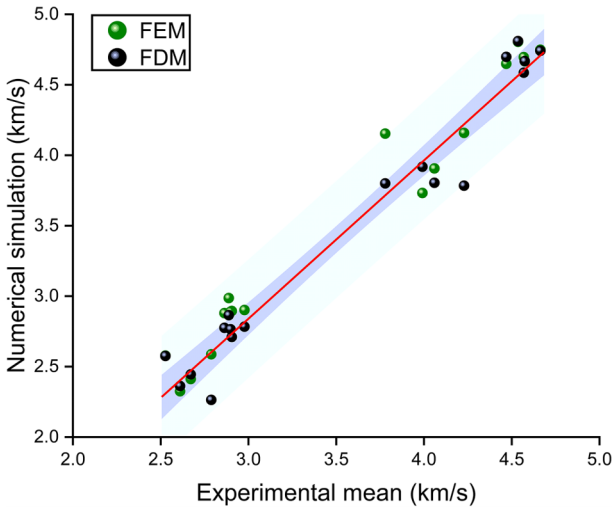

Figure 11. Correlation analysis of FEM and FDM wave velocities with the experimental ones.

5.2 The influence of CT resolution on pressure-dependent responses

To evaluate the effect of CT resolution on simulations, we calculate the relative errors between the measured and predicted (FEM and FDM) values at each effective pressure. At both resolutions, the arithmetic means of the errors in elastic velocities (V_P and V_S) simulated by the two methods for the two sets of samples are calculated. These averages preserve the overall error trend and show the pressure dependence of the two data sets across different resolutions.

Fig. 12 shows two groups of experimental samples, the mean relative errors between the measured V_P and V_S and those predicted by FEM and FDM simulations across a range of effective pressures. The errors in group I (A–D, high resolution) are smaller in the low-pressure range, while group II (E–I, low resolution) exhibits lower errors at high pressures. This difference may be relevant to the accuracy of CT resolution in characterizing microstructures.

High-resolution CT images capture more details of micropores, pore throats and grain boundaries, which better reflect the inhomogeneity of the rock at lower pressures. Consequently, simulation accuracy improves at this stage. As pressure increases, micropores and microfractures gradually close and the boundaries become flattened; as a result, the numerical model can increasingly not describe the state of the rock, leading to greater error.

On the contrary, the error for group II (low resolution) is higher at low pressures. However, as pressure increases, the rock gradually becomes more homogeneous and is better described by the low-resolution model, resulting in decreased error. Moreover, the errors at medium to high pressures are less than 5 per cent.

Overall, the results demonstrate the importance of CT scan resolution in characterizing rock microstructures. High-resolution captures more details (corresponding to low pressures), while low resolution cannot detect all microscopic structures.

6 CONCLUSIONS

We estimate the wave properties of tight sandstones using a reformulated DRP method, including mineral boundaries. We examine nine tight sandstone cores from the Shaximiao Formation in the Sichuan Basin and the Chang 7 Member of the Yanchang Formation in the Ordos Basin. XRD, CT scanning and ultrasonic measurements are used to determine the elastic properties, mineral composition and velocities V_P and V_S as functions of effective pressure under gas- and water-saturated conditions. The results show that wave velocities increase with pressure. Elastic wave velocity simulations are performed using FEM and FDM. The results show that the DRP, which considers mineral phases, is effective in estimating rock properties. The accuracy of numerical simulation depends on the resolution of the CT scan and can reflect and correlate with pressure. High resolution offers advantages for simulations at low pressures, better describing the rock microstructure. This approach could provide effective technical support for the detailed characterization of tight sandstone reservoirs.

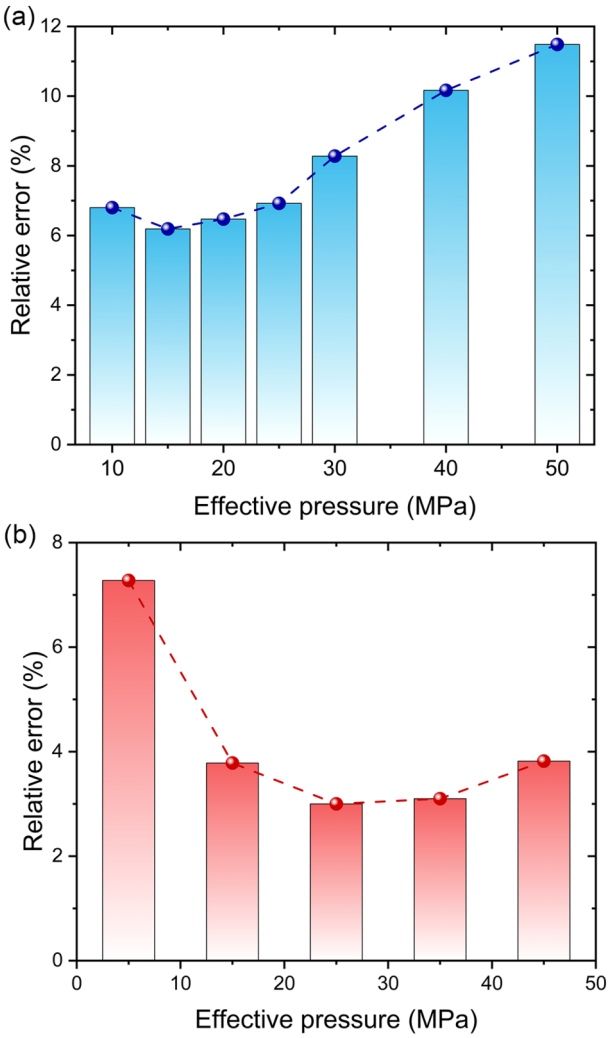

Figure 12. Comparison of mean relative errors between measured and simulated wave velocities at different pressures for the two sample groups. The bars represent the mean relative error and the dashed lines with markers illustrate the corresponding trends. **(a)** group I and **(b)** group II.

DATA AVAILABILITY

The data used in this paper could be obtained through a request to the corresponding author.

ACKNOWLEDGMENTS

The work was supported by the National Natural Science Foundation of China (42504119 and 42174161) and the Natural Science Foundation of Jiangsu Province (BK20251483). The authors gratefully acknowledge the computing time granted by the John von Neumann Institute for Computing (NIC) and provided on the supercomputer JUWELS at the Jülich Supercomputing Centre (JSC). This work was carried out under project ID wave-indent.

SUPPORTING INFORMATION

Supplementary data are available at *GJIRAS* online.

Figure S1. 3-D greyscale images of the nine samples

Figure S2. RVE analyses of the remaining samples from Group I: **(a)** Sample B, **(b)** Sample C and **(c)** Sample D.

Figure S3. RVE analyses of the remaining samples from Group II: **(a)** Sample F, **(b)** Sample G, **(c)** Sample H and **(d)** Sample I.

Figure S4. Convergence of the conjugate gradient method: Gradient norm (left axis) and energy change (right axis), illustrated using sample E.

Figure S5. Comparisons of averages of the measurements with simulations. P- **(a)** and S-wave velocities **(b)** .

CONFLICT OF INTEREST

The authors declare no conflicts of interest relevant to this study.

REFERENCES

Ahmad, R., Liu, M., Ortiz, M., Mukerji, T. & Cai, W., 2023. Computation of effective elastic moduli of rocks using hierarchical homogenization, *J. Mech. Phys. Solids,* **174,** 105–268.

Alkhimenkov, Y., 2025. Digital rock physics: calculation of effective elastic properties of heterogeneous materials using graphical processing units (GPUs), *Comput. Geosci.,* **194,** 105–749.

Andhumoudine, A.B., Nie, X., Zhou, Q., Yu, J., Kane, O.I., Jin, L. & Djaroun, R.R., 2021. Investigation of coal elastic properties based on digital core technology and finite element method, *Adv. Geo-Energy Res.,* **5**(1), 53–63.

Andrä, H. *et al.* 2013a. Digital rock physics benchmarks—Part I: imaging and segmentation, *Comput. Geosci.,* **50,** 25–32.

Andrä, H. *et al.* 2013b. Digital rock physics benchmarks—Part II: computing effective properties, *Comput. Geosci.,* **50,** 33–43.

Balcewicz, M., Siegert, M., Gurris, M., Ruf, M., Krach, D., Steeb, H. & Saenger, E.H., 2021. Digital rock physics: a geological driven workflow for the segmentation of anisotropic Ruhr sandstone, *Front. Earth Sci.,* **9,** 673–753.

Berg, C.F., Lopez, O. & Berland, H., 2017. Industrial applications of digital rock technology, *J. Pet. Sci. Eng.,* **157,** 131–147.

Beucher, S. & Meyer, F., 2018. The morphological approach to segmentation: the watershed transformation, *Mathematical Morphology in Image Processing,* pp. 433–481, CRC Press .

Cao, G., Lin, M., Zhang, L., Ji, L. & Jiang, W., 2024. Numerical simulation of the dynamic migration mechanism and prediction of saturation of tight sandstone oil, *Sci. China Earth Sci.,* **67**(1), 179–195.

Carcione, J.M., 2022. *Wavefields in Real Media: Theory and Numerical Simulation of Wave Propagation in Anisotropic, Anelastic, Porous and Electromagnetic Media,* 4th edn, Elsevier.

Chen, Q., Li, W., Gao, Y., Guo, Y., Feng, J., Zhang, D., Cao, H. & Liang, J., 2007. The deep-lake deposit in the Upper Triassic Yanchang Formation in Ordos Basin, China and its significance for oil-gas accumulation, *Sci. China Ser. D-Earth Sci.,* **50**(Suppl 2), 47–58.

Dong, S., Zeng, L., Xu, C., Dowd, P., Gao, Z., Mao, Z. & Wang, A., 2019. A novel method for extracting information on pores from cast thin-section images, *Comput. Geosci.,* **130,** 69–83.

Gao, J., Han, W., He, Y., Zhao, H., Li, H., Zhang, Y. & Xu, Z., 2021. Seismic wave equations in tight oil/gas sandstone media, *Sci. China Earth Sci.,* **64**(3), 377–387.

Gassmann, F., 1951. Elastic waves through a packing of spheres, *Geophysics,* **16**(4), 673–685.

Guo, Z.Q., Qin, X.Y. & Liu, C., 2023. Quantitative characterization of tight gas sandstone reservoirs using seismic data via an integrated rock-physics-based framework, *Pet. Sci.,* **20**(6), 3428–3440.

Hafiz, D.A., Sheta, W.M., Bayoumi, S. & Youssef, B.A., 2011. A new approach for 3d range image segmentation using gradient method, *J. Comput. Sci.,* **7**(4), 475.

Hill, R., 1952. The elastic behaviour of a crystalline aggregate, *Proc. Phys. Soc. A,* **65**(5), 349.

Hill, R., 1963. Elastic properties of reinforced solids: some theoretical principles, *J. Mech. Phys. Solids,* **11**(5), 357–372.

Kadyrov, R. *et al.* 2022. Digital rock physics: defining the reservoir properties on drill cuttings, *J. Pet. Sci. Eng.,* **210,** 110–063.

Kang, J., Li, N.Y., Zhao, L.Q., Xiong, G., Wang, D.C., Xiong, Y. & Luo, Z.F., 2022. Construction of complex digital rock physics based on full convolution network, *Pet. Sci.,* **19**(2), 651–662.

Karimpouli, S. & Tahmasebi, P., 2016. Conditional reconstruction: an alternative strategy in digital rock physics, *Geophysics,* **81**(4), D465–D477.

Ketcham, R.A., 2025. New watershed methods for isolating and characterizing discrete objects in 3D data sets, *Tomogr. Mater. Struct.,* **7,** 100–043.

Li, J., Wang, H., Wu, Z., Zhong, A., Yang, F., Meng, X. & Liu, Y., 2024. Mesoscale migration of oil in tight sandstone reservoirs by multi-field coupled two-phase flow, *Mar. Pet. Geol.,* **161,** 106–684.

Madonna, C., Quintal, B., Frehner, M., Almqvist, B.S., Tisato, N., Pistone, M., Marone, F. & Saenger, E.H., 2013. Synchrotron-based X-ray tomographic microscopy for rock physics investigations, *Geophysics,* **78**(1), D53–D64.

Mavko, G., Mukerji, T. & Dvorkin, J., 2020. *The Rock Physics Handbook,* Cambridge University Press.

Otsu, N., 1975. A threshold selection method from gray-level histograms, *Automatica,* **11,** 23–27.

Pang, M., Ba, J., Carcione, J.M., Balcewicz, M., Siegert, M., Tang, G. & Saenger, E.H., 2025. Structural and elastic properties of carbonate rocks with different pore types based on digital and theoretical rock physics, *J. Geophys. Res.: Solid Earth,* **130**(3), e2024JB030538.

Pang, M., Ba, J., Carcione, J.M., Balcewicz, M., Yue, W. & Saenger, E.H., 2022. Acoustic and electrical properties of tight rocks: a comparative study between experiment and theory, *Surv. Geophys.,* **43**(6), 1761–1791.

Pang, M., Ba, J., Wu, C.F., Carcione, J.M. & Müller, T., 2023. Acoustic-electrical properties and rock physics models for shale-oil formations: prediction of reservoir properties of interbedded sandstone and shale layers, *Appl. Geophys.,* **19**(4), 485–502.

Pang, M., Balcewicz, M., Ba, J., Carcione, J.M., Siegert, M. & Saenger, E.H., 2024. Acoustical-electrical models of tight rocks based on digital rock physics and double-porosity theory, *Geoenergy Sci. Eng.,* **235,** 212–634.

Reuss, A., 1929. Berechnung der Fließgrenze von Mischkristallen anhand der plastizitätsbedingung für Einkristalle, *Z. Angew. Math. Mech.,* **9**(1), 49–58.

Saenger, E.H. & Bohlen, T., 2004. Finite-difference modeling of viscoelastic and anisotropic wave propagation using the rotated staggered grid, *Geophysics,* **69**(2), 583–591.

Saenger, E.H., Gold, N. & Shapiro, S.A., 2000. A rotated staggered grid finite-difference scheme for 3-D elastic wave propagation, *Geophysics,* **65**(5), 1612–1620.

Saenger, E.H., Krüger, O.S. & Shapiro, S.A., 2004. Effective elastic properties of randomly fractured soils: 3D numerical experiments, *Geophys. Prospect.,* **52**(3), 183–195.

Saenger, E.H., Lebedev, M., Uribe, D., Osorno, M., Vialle, S., Duda, M., Iglauer, S. & Steeb, H., 2016. Analysis of high-resolution X-ray computed tomography images of Bentheim sandstone under elevated confining pressures, *Geophys. Prospect.,* **64**(4), 848–859.

Saenger, E.H. & Shapiro, S.A., 2002. Effective velocities in fractured media: a numerical study using the rotated staggered finite-difference grid, *Geophys. Prospect.,* **50**(2), 183–194.

Saxena, N., Hows, A., Hofmann, R., Alpak, F.O., Dietderich, J., Appel, M., Freeman & De Jong, H., 2019. Rock properties from micro-CT images: digital rock transforms for resolution, pore volume, and field of view, *Adv. Water Resour.,* **134,** 103–419.
Sobel, I., 1995. *An Isotropic 3×3×3 Volume Gradient Operator, Technical report,* Hewlett-Packard Laboratories.
Supiyandi, S., Panggabean, T., Ramadhan, N., Dewi, S.R. & Yusra, S., 2024. Deteksi tepi sederhana pada citra menggunakan operator sobel, *Repeater,* **2**(3), 43–56.
Tan, M., Su, M., Liu, W., Song, X. & Wang, S., 2021. Digital core construction of fractured carbonate rocks and pore-scale analysis of acoustic properties, *J. Pet. Sci. Eng.,* **196,** 107–771.
Voigt, W., 1966. *Lehrbuch der Kristallphysik: (mit Ausschluss der Kristalloptik),* Bibliotheca mathematica Teubneriana, Bd. 12, Johnson Reprint.
Wang, J., Mohr, S., Feng, L., Liu, H. & Tverberg, G.E., 2016. Analysis of resource potential for China's unconventional gas and forecast for its long-term production growth, *Energy Policy,* **88,** 389–401.
Wang, Y. & Rahman, S.S., 2023. Numerical modelling of reservoir at pore scale: a comprehensive review, *J. Comput. Phys.,* **472,** 111–680.
Wu, H., Dong, X., Xu, Y., Xiong, G., Shen, Z. & Wang, Y., 2021. Seepage mechanism of tight sandstone reservoir based on digital core simulation method, *Appl. Sci.,* **11**(9), 3741.
Yang, T., Li, X., Yang, Y., Wen, L., Cao, Z., Wang, X., Zhang, S. & Liang, Q., 2024. Evolution from shallow-water deltas to fluvial fans in lacustrine basins: a case study from the Middle Jurassic Shaximiao Formation in the central Sichuan Basin, China, *Sedimentology,* **71**(3), 1023–1055.
Zhang, L., Ba, J., Li, C., Carcione, J.M. & Zhou, F., 2022. Joint inversion of the unified pore geometry of tight sandstones based on elastic and electrical properties, *J. Pet. Sci. Eng.,* **219,** 111–109.
Zhang, L., Jing, W., Yang, Y., Yang, H., Guo, Y., Sun, H., Zhang, T. & Yao, J., 2019. The investigation of permeability calculation using digital core simulation technology, *Energies,* **12**(17), 3273.
Zhang, S., Liu, J., Li, L., Kassabi, N. & Hamdi, E., 2024. Petrophysical and geochemical investigation-based methodology for analysis of the multilithology of the Permian Longtan formation in southeastern Sichuan basin, SW China, *Energies,* **17**(4), 766.
Zhu, J., Zhao, L., Zhu, W. & Geng, J., 2025. Joint use of multiscale digital rock physics and effective medium theory to model elastic properties of shale reservoir, *Geophysics,* **90**(4), MR323–MR334.
Zou, C., Zhu, R., Liu, K., Su, L., Bai, B., Zhang, X., Yuan, X. & Wang, J., 2012. Tight gas sandstone reservoirs in China: characteristics and recognition criteria, *J. Pet. Sci. Eng.,* **88,** 82–91.